Paired photoelectrochemical conversion of CO_2/H_2O and glycerol at high rate

Ádám Balog , Egon Kecsenovity, Gergely F. Samu , Jie He, Dávid Fekete & Csaba Janáky ✉

Photoelectrochemistry holds the promise of directly converting sunlight to valuable chemical products. Photoelectrochemical (PEC) methods, however, lag behind their electrochemical counterparts in terms of current density. In this work, we demonstrate that, by using concentrated sunlight, we can achieve current densities similar to electrochemical methods, but with lower energy input. Specifically, we combined the direct PEC oxidation of glycerol with the dark hydrogen evolution or CO_2 reduction in a membrane-separated continuous-flow PEC cell. We achieved over 110 mA cm^{-2} photocurrent density, which is at least an order of magnitude larger than those typically reported in the literature. We demonstrated that the product distribution of glycerol oxidation is notably different in PEC and electrochemical scenarios at the same current density, and the parasitic oxygen evolution reaction can be suppressed in the PEC case. This approach raises opportunities to drive complex electrochemical reactions in a more selective manner.

Electrosynthesis is having its renaissance and several industrial processes are being electrified[1,2]. A key opportunity to unleash the full potential of electrocatalysis is the coupling of two electrochemical reactions, each of which produces industrially useful products[3]. The concept of paired electrolysis builds on the successful history of chlor-alkali electrolysis, where chlorine and hydrogen are cogenerated. A recent technoeconomic analysis of 295 electrochemical coproduction combinations evaluated the economic feasibility of CO_2 reduction (CO_2R) technology combined with value-added organic oxidation and has found several profitable candidate combinations[4]. Despite the impressive achievements, the following key challenges and bottlenecks hinder the electrification of many processes: selective catalysts are necessary, which avoid the parasitic hydrogen evolution reaction (HER) in the case of cathodic processes and allow selective organic oxidation reactions, instead of CO_2 and O_2 formation as anodic reactions; low-cost catalysts are needed to enable easy and cost-efficient scale-up of the eventually developed technologies. This issue can already be seen for polymer electrolyte membrane water electrolysis, especially considering the steep growth in Ir cost[5]. Catalysts shall allow operation at low overpotential, which results in high energy efficiency. The reaction rate and selectivity are inherently coupled in the electrochemical scenario because of the Butler–Volmer relationship. This means that the current density and the electrode potential cannot be changed independently; therefore, ensuring high reaction rate often sacrifices the selectivity (that is, intended product distribution). This is especially problematic for reactions and catalysts where even small changes in the electrode potential alter the product distribution completely (for example, in the case of CO_2R to C2+ products on Cu)[6,7].

Considering the above challenges, the question comes, whether photoelectrochemical (PEC) methods can overcome some of these challenges. So far, PEC reduction studies have been mostly limited to water splitting (H$_2$ generation)[8], CO_2R to C1 products[9–11] and most recently N$_2$ reduction to NH$_3$ (ref. 12). Although in principle integrated PEC methods can provide a cost-efficient alternative to the photovoltaic + electrochemical (PV + EC) approach[13–15], they are not really competitive for the above reactions, according to our recent literature review in which more than 300 papers were analysed from the recent past[16]. Small conversion rates and low conversion efficiencies together with low durability are all of concern. At the same time, we found that PEC methods often outperform their photochemical and

Department of Physical Chemistry and Materials Science, Interdisciplinary Excellence Centre, University of Szeged, Szeged, Hungary.
✉e-mail: janaky@chem.u-szeged.hu

PV + EC counterparts in terms of selectivity[16]. Note that this resonates with the key lesson learned from natural photosynthesis where exceptionally high selectivity can be obtained.

PEC processes in continuous-flow cells have been mostly restricted to water splitting[17]. As for CO_2 conversion, most PEC studies used a photoanode for oxygen evolution reaction (OER), and CO_2R occurred at the dark cathode[10,18–23]. The lack of cell and system developments have been hindering the proper assessment of different PEC reactions. When moving from batch-type experiments to continuous-flow cells, the following parameters have to be considered: the type of reactant feed used (liquid or gas), which electrode(s) is (or are) illuminated, whether an ion-exchange membrane is used or not, mass transport conditions, cell impedance, pressure capability, applicable temperature and flow rate. Furthermore, one has to consider the interplay of the two half reactions, how to match the current densities, provide an optimal pH and temperature range and so on. Finally, to ensure proper reactant feed, the use of gas diffusion electrodes (GDEs) is highly recommended for gas phase reactants.

PEC valorization of organic wastes is also in its infancy, mostly focusing on wastewater treatment via complete mineralization. When CO_2R is coupled with OER as the anode process, OER consumes approximately 90% of the electricity input in the electrochemical scenario[24]. This issue can be addressed by coupling other anodic oxidation reactions with lower or at best zero[25] voltage requirement and higher-value products. As an example, oxidation of glycerol[7] (a by-product of biodiesel and soap production in large quantities, a few million metric tons annually) can lower electricity consumption by over 50% (ref. 24). In addition, high-value products can be obtained, including formic acid, acrolein, 1,3-dihydroxyacetone or 3-hydroxypyruvic acid, glyceraldehyde and lactic acid[24,26]. PEC oxidation of methanol, benzyl alcohol, 5-hydroxymethylfurfural (HMF) was also performed on n-type semiconductor photoanodes. A notable feature was the high selectivity values (approaching 100% in certain instances)[27–29]. None of these processes were performed in continuous flow or under concentrated sunlight, therefore, the achieved photocurrent values remained low (up to 4 mA cm^{-2}).

Coupling alternative anodic oxidation reactions (that is, not OER) with lower electricity needs and higher-value products is an increasingly studied approach in electrosynthesis[4,24,30,31]. This strategy offers opportunities for PEC methods as well, because there will be no need to cope with the energy need, and the sluggish kinetics of OER, therefore a broader pool of semiconductors can be used. At the same time, the complete mineralization (that is, CO_2 formation) of the organic molecules has to be avoided, because that would undermine the environmental relevance of the whole process. Although a few examples demonstrated such coupling, only two of them focused on the CO_2 at the cathode[25,32]. Furthermore, they were performed in batch cells, which hinders future scale-up efforts. Combined biomass valorization and H_2 production was demonstrated, where the oxidation of HMF into 2,5-furandicarboxylic acid occurred at the anode of a PEC cell[29]. Using a molecular redox mediator a near-quantitative yield and 100% Faradaic efficiency (FE) was achieved. In another, bio-PEC approach[33], a Mo:BiVO$_4$ photoanode was employed to generate H_2O_2 in situ, which simultaneously supplied peroxygenases to drive a selective hydroxylation reaction.

To decrease the footprint of PEC technologies to a level that is competitive with electrochemical processes, the current densities have to be increased substantially (that is, by order(s) of magnitude)[34,35]. Using concentrated sunlight is the only way to increase the current density from the theoretically achievable limits (for example, 45 mA cm^{-2} for Si with a bandgap of 1.1 eV) to industrially relevant values. The solar power input can be concentrated up to 1,000 sun, which in combination with proper buried photovoltaic cells already allowed current densities similar to those in industrial electrolysers. For water splitting, 0.88 A cm^{-2} current density was demonstrated with a solar-to-hydrogen

conversion efficiency over 15%, under concentrated solar irradiation (up to 474 kW m^{-2})[36]. A similarly integrated PV + EC setup was developed for CO_2R as well, where 17% solar-to-CO conversion efficiency was achieved at 150 mA cm^{-2} current density[37]. Similar arrangements can be envisioned for other high-value PEC processes, where proper electrode development, light and thermal management, and sufficient stability can be ensured.

On the basis of all the above-discussed advantages and disadvantages, here we present a PEC cell design containing an n-type silicon-based photoanode and dark gas diffusion cathode to perform the combined reduction of water or CO_2 at the cathode with the oxidation of glycerol at the anode. We use concentrated sunlight and a continuous-flow PEC cell to decrease the cell voltage and to achieve selective formation of glycerol oxidation products without OER, which is difficult to implement via electrochemical methods. We demonstrate that PEC methods can result in lower voltage requirement and higher selectivity at high current density, by decoupling the overpotential and the number of generated charge carriers.

Results
The design of the PEC cell
All experiments presented in this paper were performed in a custom-designed flow PEC cell (Fig. 1). This is a markedly different design from the traditional PV + EC reactors, where a photovoltaic cell is connected to the electrodes through external wires. In our case, the whole photoanode is immersed in the electrolyte and the catalyst covered part of the electrode is the only electrochemically active part of the PEC assembly (Supplementary Fig. 1 and the description in the Supplementary Note 1). The disruptive potential of this cell is that front illumination can be used during the experiments, which allows the application of non-transparent substrates and expands the list of suitable semiconductors (such as silicon (Si)). Note that front illumination can overcome two limitations that strongly affect the PEC performance in flow cells operated with backside illumination. On one hand, more light can reach the photoactive material, which is a limiting factor in the case of gas diffusion layers as supporting electrodes. On the other hand, the use of perfectly transparent fluorine doped tin oxide or indium doped tin oxide introduces higher cell resistance, due to the lower conductivity of these substrates. Another advantage of this PEC cell is that the temperature can be precisely controlled by a tempered inert medium flowing through a fluid chamber designed in the end plate. There are examples in the literature where the cell temperature is set by the recirculated electrolyte[38]; however, at lower flow rates the accurate temperature cannot be maintained in this way. Moreover, concentrated sunlight heats the cell continuously, which makes the temperature control even more important.

PEC CO_2 reduction and glycerol oxidation at high currents
To achieve selective conversion of reactants in both half reactions, the most important parameter that needs to be considered is the local chemical environment[39]. In this regard, the electrochemical oxidation of glycerol is favoured in alkaline media because the first deprotonation step (alcohol to alkoxide) is base catalysed[40]. Therefore, a strongly basic solution should be used as the anolyte, where the type of alkali cation can also have an important role in the glycerol oxidation reaction[41]. These cations can interact with the intermediates thereby affecting selectivity. As for CO_2R, the presence of large cations (such as caesium) increases the partial current density for CO formation and at the same time suppresses the parasitic H_2 production[42]. This can happen because of the cation crossover from the anode to the cathode through the anion-exchange membrane (AEM), which changes the local chemical environment on the cathode side and promotes the CO_2R (ref. 43). Considering all of these observations, glycerol containing CsOH electrolyte was employed in all experiments.
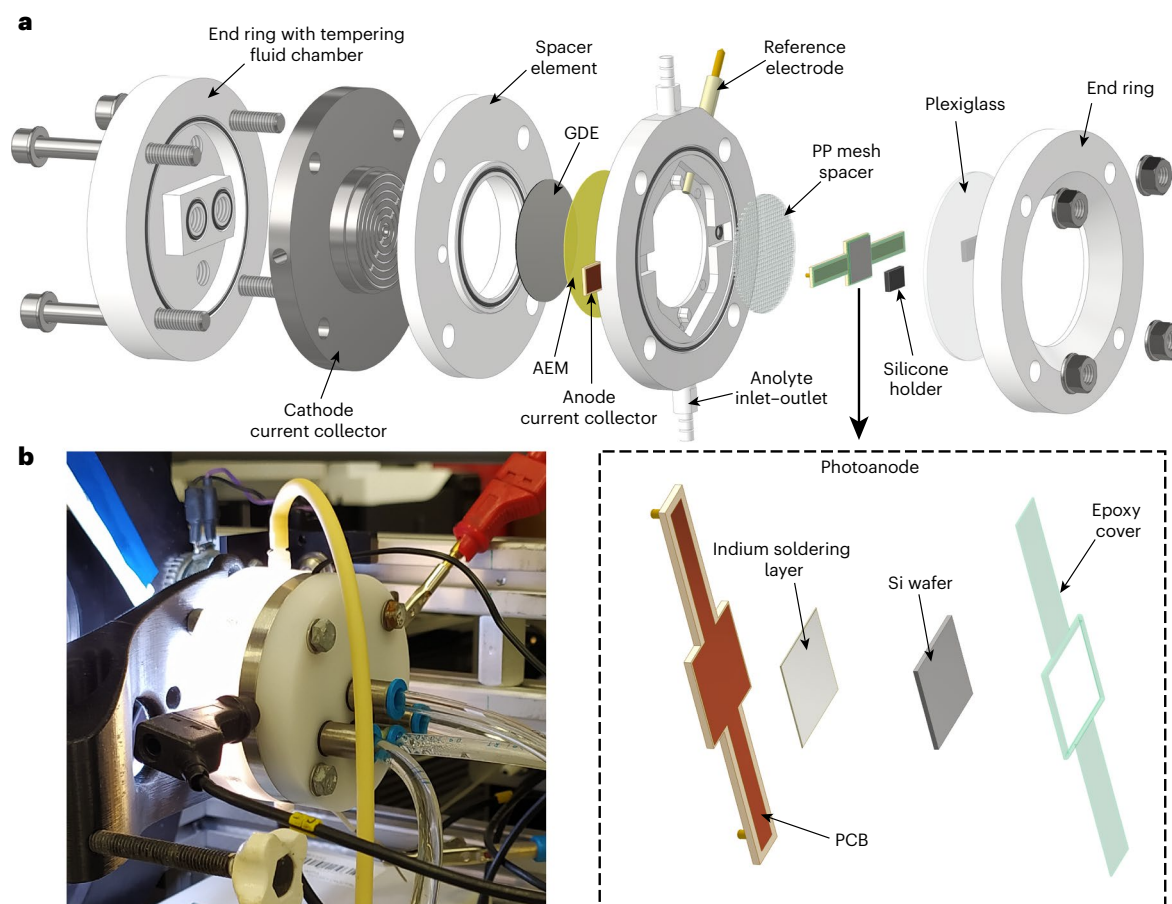
Fig. 1 | Design of the PEC cell. a, Schematic exploded view of the PEC cell with the detailed structure of the photoanode. **b**, A photograph of the PEC cell under operation. AEM, anion-exchange membrane; GDE, gas diffusion electrode; PP, polypropylene; PCB, printed circuit board.

The PEC behaviour of the custom-designed flow cell was first probed by photovoltammetry (Fig. 2a) in the potential range between −0.2 and 1.0 V (versus Ag/AgCl) using concentrated (10 sun) solar illumination (the solar spectrum is shown in Supplementary Fig. 2a). The onset potential of the photocurrent related to glycerol oxidation was around 0 V (versus Ag/AgCl), then a continuous increase was observed with a photocurrent maximum of more than 110 mA cm^{-2}. This photocurrent density value is about an order of magnitude higher compared to precedent literature reports on PEC glycerol oxidation, which are all below 10 mA cm^{-2} (Fig. 2b)[26,44–52]. Moreover, the observed photocurrent densities in this work are comparable with the dark currents achieved with the best Ni-containing catalysts (Ni(OH)$_2$ (ref. 41) and Ni−Mo−N, ref. 53) (Fig. 2b), even though the electrochemical surface area is much lower in our case (we deposited the Ni nanoparticles on a flat Si wafer, while in the two literature examples, Ni(OH)$_2$ nanoflakes were deposited on Ni foam, and Ni−Mo−N nanoplate structure—composed of nanoparticles—was grown on carbon fibre cloth). In addition, the onset potential achieved with the photoelectrode is much lower, as the photopotential of Si is harnessed (later). At the same time, there are recent reports on dark electrocatalytic studies, where higher current densities have been achieved in different organic oxidation reactions[31].

A potentiostatic measurement was performed at 1.0 V (versus Ag/AgCl) to check the stability of the photocurrent (Fig. 2c). During this experiment, the product distribution was also analysed at both the cathode and anode sides (Fig. 2d). Then, 95% CO and 5% H$_2$ were identified as the cathodic products (that is, FE), while a mixed product distribution was detected in the anolyte with formate, glycerate, glycolate, oxalate, tartronate and lactate (the exact FE of each

product was calculated with the equations given in Supplementary Note 2 using the electron numbers in Supplementary Table 1). The total FE belonging to stable (unreactive) products was roughly 85% on the anode side, which is one of the highest values compared to the reported FEs in the literature related to glycerol oxidation, especially at high current densities (in many cases, FE values are not even shown, only selectivity data are presented)[41,54,55]. The remaining roughly 15% FE can be rooted in the formation of multiple by-products. If there is CO$_2$ formation (via formate oxidation) during the oxidation process, it can dissolve immediately in the alkaline solution producing carbonate. Carbonate ions are difficult to quantify in the strongly basic medium, especially at such low concentrations. To examine the possibility of PEC formate oxidation to carbonate, formate containing CsOH was used as the anolyte in a control experiment. In this case, the two possible processes are the oxidation of formate and the OER. We proved that there is no formate oxidation on our catalyst, as the concentration of formate was not decreased after the PEC reaction (Supplementary Fig. 3). Crossover of the anodic products to the cathode through the AEM, can also lead to an apparent loss in the FE. While this is unlikely, as the cathode is negatively charged, so the anions have a potential barrier in that direction, we have quantified their amount. The total FE related to the product crossover from the anode to the cathode was only 1.10 ± 0.24%.

Furthermore, some C3 and C2 oxidation products (such as glyceraldehyde, dihydroxyacetone and glycolaldehyde) are not chemically stable under highly basic conditions, they can decompose spontaneously to produce formate and other products[55]. These by-products appear on the ion chromatogram as small peaks[55] (indicated by the
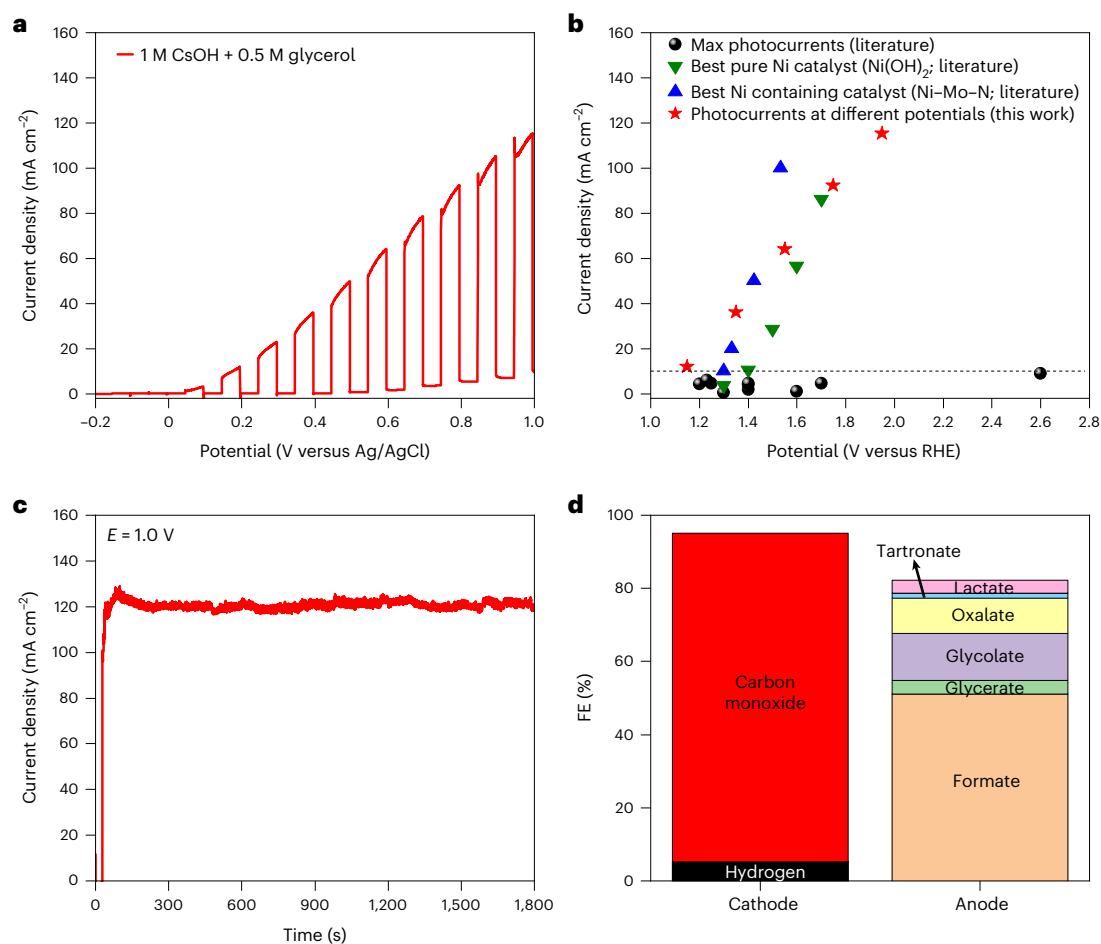
Fig. 2 | PEC properties and product distribution during the paired conversion of glycerol and CO_2. a, Photovoltammogram of a Ni-covered Si photoanode. **b**, Comparison of glycerol oxidation photocurrents achieved in this work (red stars) with the maximum photocurrents from the literature[26,44–52] (black circles). The best Ni-containing dark catalysts ($Ni(OH)_2$ (ref. [41]) and Ni–Mo–N (ref. [53]) are also marked on this figure (green and blue triangles). **c**, Potentiostatic measurement at 1.0 V versus Ag/AgCl anode potential for 30 min. **d**, Cathode and anode product distribution at 1.0 V versus Ag/AgCl. The experiments were performed using a solar simulator (AM 1.5) as the light source operated at 1,000 mW cm^{-2} (10 sun). The anolyte was 0.5 M glycerol containing 1.0 M CsOH. CO_2R was performed on the cathode side using 25 cm^3 min^{-1} CO_2 flow, while the anolyte was non-recirculated and the flow rate was 2 cm^3 min^{-1}. The temperature of the cell and the anolyte was 35 °C. The missing FE on the anode side (**d**) is related to dihydroxyacetone, glyceraldehyde and oxygen. RHE, reversible hydrogen electrode.

black arrows in the inset of Supplementary Fig. 4) beside the main products (Supplementary Fig. 4) that are not evaluated during the calculation of the FEs. To further verify that these unstable by-products are really produced in the PEC glycerol oxidation reaction and to find out exactly which intermediates are involved in this process, several control measurements were performed and will be discussed below. Finally, there is always a possibility for the parasitic OER where another reactive intermediate (O_2) is formed. These intermediates together are now noted as reactive products and account for the remaining roughly 15% FE in Fig. 2d.

As a partial conclusion, the paired PEC CO_2R and glycerol oxidation can be performed effectively without the complete mineralization of glycerol (that is, CO_2 formation). On the other hand, when CO_2R occurs on the cathode side, there is an unintended extra source of carbonate through the AEM[43,56]; therefore, an excess amount of carbonate will be in the anolyte, which may affect the product distribution (and also the stability, as it is shown below). Because of this, HER was performed on the cathode side in those experiments where the anolyte composition was studied. In these cases, a continuous argon flow was fed to the cathode to exclude the other possible processes (for example, oxygen reduction).

Effect of the operational parameters

Ni catalysed glycerol oxidation starts simultaneously with the transformation of $Ni(OH)_2$ to NiOOH, which is responsible for the catalytic activity in this reaction[57,58]. NiOOH is a widely used material in OER as well, which raises the possibility of the competition between the two processes. Because of this, the PEC behaviour of the Ni-coated Si photoanode was examined in 1.0 M CsOH with and without the presence of glycerol (Fig. 3a). The oxidation of glycerol started at 200 mV lower potential (~0 V versus Ag/AgCl) compared to OER (~0.20 V versus Ag/AgCl), while the maximum photocurrent density recorded at 1.0 V (versus Ag/AgCl) was two times higher (105.8 versus 57.0 mA cm^{-2}). This signals that glycerol oxidation is both thermodynamically and kinetically more favoured compared to water oxidation. As the next step, the intensity dependence of the photocurrent was determined (Fig. 3b). There was a linear relationship between the photocurrent and the intensity (at least in the range between 1 and 10 sun as shown in Supplementary Fig. 2b), which shows that more charge carriers can be generated using higher light intensities and, most importantly, these carriers can be extracted.

The effect of two external parameters were also examined, namely the effect of temperature (Fig. 3c) and glycerol concentration (Fig. 3d).
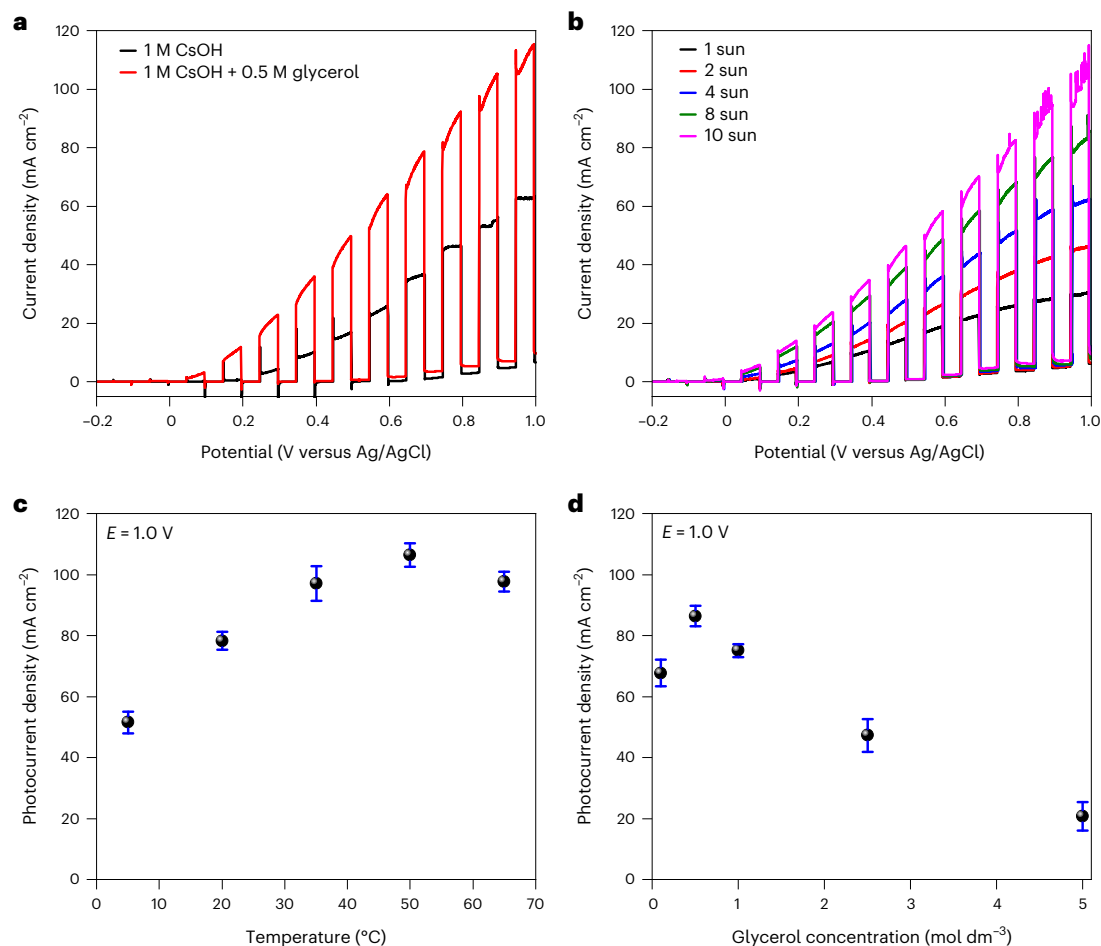
Fig. 3 | PEC behaviour and its dependence on the operational parameters.
a,b, Photovoltammograms of Ni-covered Si photoanode recorded in pure and
0.5 M glycerol containing 1.0 M CsOH (**a**) and at five different light intensities
in 0.5 M glycerol containing 1.0 M CsOH (**b**). **c,d**, Temperature (**c**) and
glycerol concentration dependence (**d**) of the photocurrent derived from the
photovoltammograms at 1.0 V versus Ag/AgCl. The experiments were performed
using a solar simulator (AM 1.5) as the light source operated at 1,000 mW cm^{-2}
(10 sun). The sweep rate was kept at 10 mV s^{-1} and the light-chopping frequency
was 0.2 Hz. HER was performed on the cathode side using 25 cm^3 min^{-1} argon
flow and the anolyte flow rate was 10 cm^3 min^{-1}. The error bars represent the
standard deviation from the average (mean), originated from three separate
measurements performed on three different Ni/Si electrodes.

A continuous photocurrent increase was observed as the temperature
was raised from 5 to 35 °C, while further increase in the temperature had
no influence on the photocurrent. Changing the glycerol concentra-
tion in the anolyte, an interesting current trend was observed. There
was an increase in the photocurrent between 0.1 and 0.5 M; however,
a decrease was measured at higher concentrations. Electrochemi-
cal impedance spectroscopy and dynamic viscosity measurements
were carried out to explain the trends in the photocurrent (Supple-
mentary Figs. 5 and 6). As both the diffusion coefficient and the ion
mobility decrease with the increasing viscosity, the alterations in the
cell resistance are a direct consequence of the change in electrolyte
viscosity. Between 5 and 35 °C, both the cell resistance and the viscos-
ity decreased, which explains the photocurrent trend perfectly (Sup-
plementary Fig. 6a,b). In the case of concentration dependence, the
cell resistance and the viscosity were almost constant up to 1.0 M and
only increased at higher glycerol amounts (Supplementary Fig. 6c,d).
By contrast, the photocurrent first increased (between 0.1 and 0.5 M),
then a decrease was observed (between 0.5 and 5.0 M). This shows
that glycerol oxidation is more favoured compared to water oxidation
(Fig. 3a). At low glycerol concentration, that is the limiting factor for the
photocurrent. As glycerol concentration increases, the photocurrent
increases in parallel, while the water oxidation is gradually suppressed.
This is confirmed by the product analysis, where more than 20% FE is
related to oxygen formation at 0.1 M (Fig. 4b) and at higher glycerol
amounts the contribution of water oxidation is undetectable. After an
optimal concentration (0.5 M), however, the anolyte viscosity deter-
mines the achievable photocurrent density. The increasing viscosity,
and therefore the limited mass transport, is the reason for the gradual
decrease in the photocurrent at the concentrations higher than the
optimal value (0.5 M).

To evaluate the effect of operational parameters on the product
distribution, potentiostatic measurements were carried out and the
anolyte composition was examined by NMR (nuclear magnetic reso-
nance) spectroscopy and ion chromatography. Six different products
were detected after the electrochemical oxidation of glycerol: for-
mate, glycerate, glycolate, oxalate, tartronate and lactate. The rela-
tive quantity of these products can be controlled by varying the cell
temperature, the concentration of glycerol and the anode potential
(Fig. 4a–c). The parasitic oxygen formation was also monitored during
these experiments by an oxygen sensor and was only detectable at the
lowest glycerol concentration (0.1 M in Fig. 4b).

To explain the changes in the product distribution at different
operational parameters, the reaction mechanism of glycerol oxida-
tion should be examined carefully (Fig. 5). According to the litera-
ture[55,59], glycerol oxidation starts with a base-catalysed deprotonation
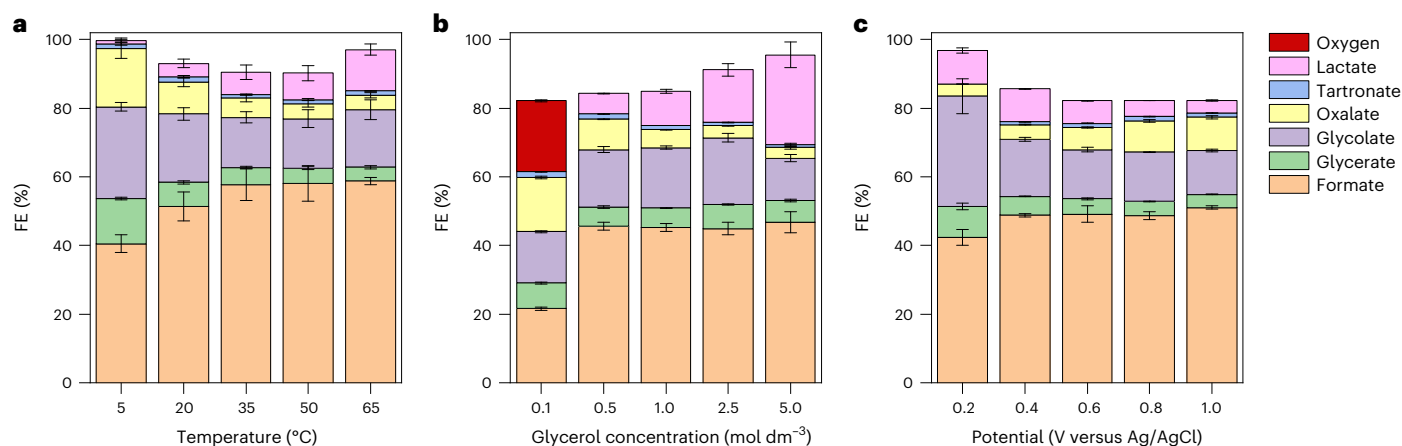step, followed by a second one with the contribution of the catalyst.

Fig. 4 | Product distribution in the anolyte and its dependence on the operational parameters. The products were analysed by NMR spectroscopy and ion chromatography after 30 min of potentiostatic measurements. **a**–**c**, The effect of temperature (0.5 M glycerol in 1.0 M CsOH, 0.6 V versus Ag/AgCl) (**a**), glycerol concentration (1.0 M CsOH, 35 °C, 0.6 V versus Ag/AgCl) (**b**) and potential (0.5 M glycerol in 1.0 M CsOH, 35 °C) (**c**) were examined. The constant parameters are indicated in parentheses. HER was performed on the cathode side using 25 cm³ min⁻¹ argon flow, while the anolyte flow rate was 10 cm³ min⁻¹. The error bars represent the standard deviation from the average (mean), originated from three separate measurements performed on three different Ni/Si electrodes. The missing FE is related to dihydroxyacetone, glyceraldehyde and oxygen.
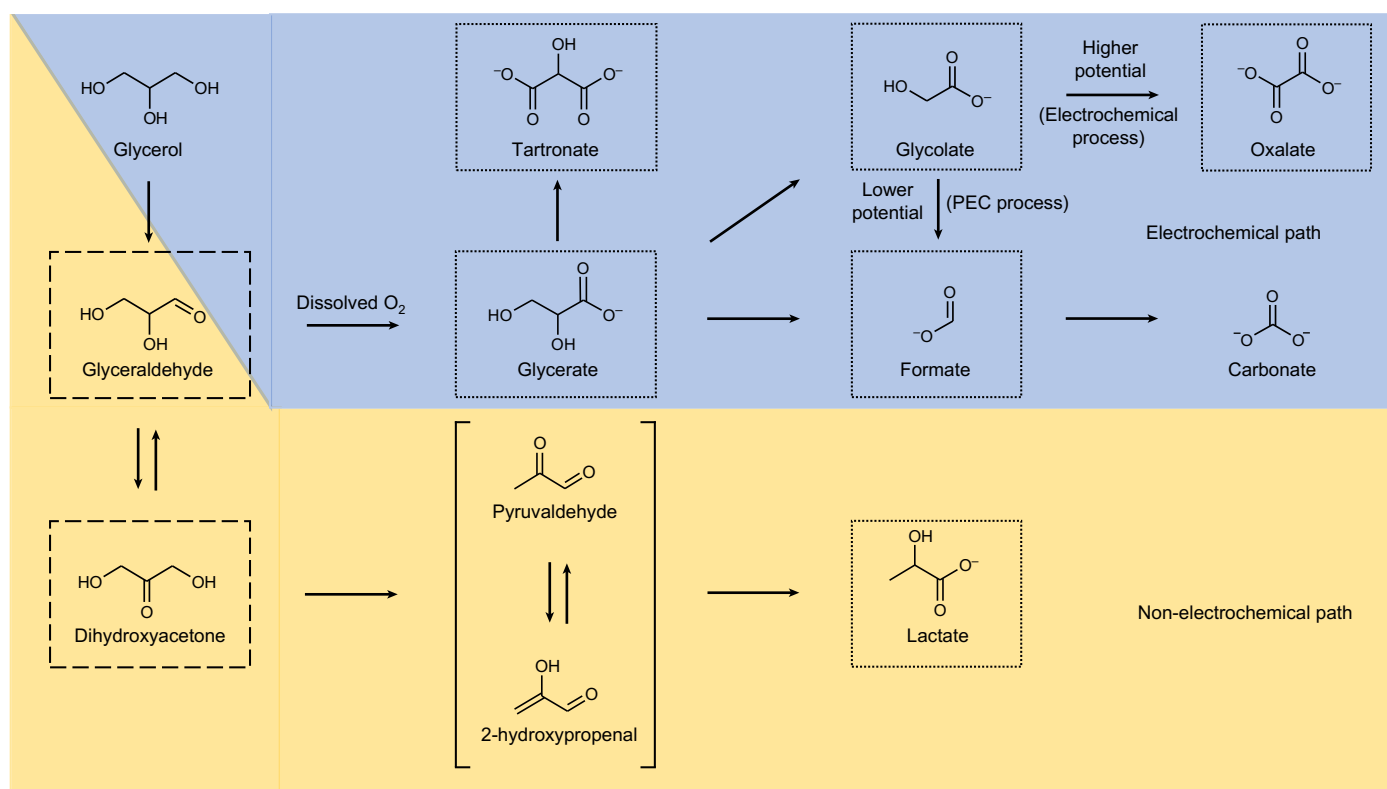

Fig. 5 | Proposed reaction pathways for glycerol oxidation in alkaline solution[54,59,72]**.** The detected products are framed by dotted lines and the unstable intermediates are framed with dashed lines.

The resulting glyceraldehyde and dihydroxyacetone are in equilibrium in alkaline solutions. The electrochemical oxidation of these reaction intermediates results in different products (marked in blue in Fig. 5), in addition, there is a non-electrochemical path as well, which consists of a dehydration and a rearrangement step, producing lactate (marked with yellow in Fig. 5). The electrochemical path can produce glycerate, tartronate, glycolate, formate, oxalate or even carbonate (this last one being an unintended product affecting the overall CO₂ balance of the coupled process; however, it does not occur in the PEC process in our system, as discussed before). This reaction pathway can be favoured by using low temperatures, low glycerol concentrations and high anode potentials (Fig. 4). Note that the amount of C3 products is very low, which is not surprising in the case of Ni catalysed glycerol oxidation in strongly alkaline media where C–C cleavage is favoured[41,55].

Higher temperatures, higher glycerol concentrations and lower anode potentials favour the non-electrochemical formation of lactate

(Fig. 4). On the basis of these observations, three conclusions can be drawn: the temperature increase has a positive effect on lactate formation (Fig. 4a), parasitic oxygen formation can completely suppress the non-electrochemical path (at the lowest concentration of glycerol in Fig. 4b) and when the electrochemical oxidation slows down (that is, lower current densities can be measured), relatively more glyceraldehyde and/or dihydroxyacetone can transform to lactate through the non-electrochemical process (Fig. 4b,c).

All the above-mentioned conclusions suggest the formation of dihydroxyacetone and/or glyceraldehyde reactive intermediates that are not stable under the experimental conditions: they are not chemically stable in highly alkaline electrolytes that manifests in their spontaneous decomposition[55], they are sensitive to dissolved oxygen and undergo a chemical oxidation resulting glycerate[60] (first step of glyceraldehyde and/or dihydroxyacetone transformation in the reaction path marked with blue in Fig. 5), they are also sensitive to high temperatures. To prove the formation of these products during the PEC reaction, the product distribution was compared in an argon deaerated and oxygen saturated anolyte under otherwise identical conditions (Supplementary Fig. 7). A yellow colour was observed in the argon deaerated electrolyte after the PEC experiment, while the oxygen saturated sample remained transparent. This suggests that at least one of the products (which has yellowish colour) is not detected in the argon deaerated samples and that is the reason for the unaccounted roughly 15% FE. Using ultraviolet–visible (UV–vis) absorbance measurements we found that the yellow colour and the missing FE come from dihydroxyacetone and glyceraldehyde (details in the Supplementary Note 3, and UV–vis absorbance spectra in Supplementary Figs. 8 and 9), but the quantification of these products is not possible as their concentrations continuously change. Moreover, when the parasitic OER can also occur (at 0.1 M concentration of glycerol in the PEC process and also in the dark oxidation: below), the exact amount of both intermediates and oxygen is unknown, as they react with each other. Consequently, dihydroxyacetone, glyceraldehyde and oxygen are all part of the reactive products that contribute to the missing FE in all figures related to anodic product distribution.

To prove that the magnitude of the current density influences the reaction pathway the most (and not the anode potential), the product distribution was compared in potentiostatic and galvanostatic experiments under 1 and 10 sun (Supplementary Note 4 and Supplementary Figs. 10 and 11). There was a slight difference in the product distribution under potential control. The difference was due to the higher FE of lactate and glycolate (Supplementary Fig. 10). By contrast, the product distribution was independent from the light intensity when the same current density was applied, even though the potential response was lower under 10 sun irradiation (Supplementary Fig. 11). This confirms the basic principle of photoelectrochemistry that the valence band position determines the energy of holes and not the applied potential.

Differences between the electrochemical and PEC scenarios

In general, PEC cells are less efficient than dark electrolysers in terms of maximum current densities (that is, reaction rates) (at least under 1 sun of irradiation as shown in Fig. 2b). A great advantage of these systems, however, lies in the lower electricity consumption (that is, lower external bias to maintain the given current density) and/or in the higher selectivity, which is especially important in the reactions where multiple products can be produced. This can be explained by the appearance of the photopotential under illumination, which lowers the onset potential of the given process, resulting in lower half-cell potential and therefore lower cell voltage. In most cases, however, the photocurrent reaches a saturation level at a certain potential, whereas the current increases monotonously in dark (unless there are mass transport limitations). Therefore, dark electrochemical cells usually outperform the PEC systems in terms of currents, but at the same time the selectivity is more difficult to control even at low current densities.

To demonstrate the differences between the two scenarios, we compared the dark and photooxidation of glycerol under otherwise identical conditions. Dark measurements were performed with a Ni sheet (acting as the catalyst layer) that was soldered to the printed circuit board (PCB) by an indium layer. Linear sweep voltammograms showed roughly 0.45 V lower onset potential of glycerol oxidation in the case of the photoelectrode, and this photopotential value was constant up to 30 mA cm^{-2}, while it became higher at higher current densities (Supplementary Table 2). This trend is due to the shoulder observed on the dark current trace that is not present in the photocurrent curve (Fig. 6a). This signals that an additional process takes place in the dark measurement over 30 mA cm^{-2} current density, which is most probably associated with water oxidation as continuous bubble formation was observed on the surface of the Ni sheet. The photopotential lowered the anode potentials in the case of the PEC setup (Fig. 6b and Supplementary Fig. 12a), and also the cell voltages (Fig. 6c and Supplementary Fig. 12b) in a similar manner.

Even more interestingly, notable differences were observed in the product distribution between the electrochemical and PEC scenarios at the same current density (Fig. 6d and Supplementary Fig. 12c). The main differences are the lower total FE of glycerol oxidation products in the case of the electrochemical process (in agreement with the literature[41,54,55]); and the higher FE of formate and lactate, as well as the lower FE of glycerate and oxalate in the PEC oxidation. Both are the direct consequences of the parasitic OER in the electrochemical scenario, competing with glycerol oxidation in the dark and the forming O_2 reacts with the intermediate products. As mentioned, glyceraldehyde and dihydroxyacetone are sensitive to dissolved oxygen and are immediately oxidized chemically to glycerate (and different other products)[60]. This is followed by the electrochemical oxidation of glycerate to glycolate and formate. Glycolate can be further oxidized to oxalate or formate. By contrast, the dark electrochemical process (at high anodic potentials) favours glycolate oxidation only to oxalate[61]. In the case of the PEC process, there is no observable oxygen formation, so in this case a part of glyceraldehyde and dihydroxyacetone can turn into lactate in the non-electrochemical step marked in yellow in Fig. 5 (especially when the photocurrent density is low). Glyceraldehyde and dihydroxyacetone can also be oxidized electrochemically to formate (this is the favoured product of glycolate oxidation at lower potentials, and therefore in the PEC process as the potential is fixed by the valence band position in this case).

To prove the participation of dissolved oxygen in the reaction, we measured its concentration during photo- and dark electrolysis at 100 mA cm^{-2} (Supplementary Fig. 13). While there is no detectable oxygen formation in the PEC reaction, it is certainly present in the dark process. Accordingly, the oxygen concentration decreased to zero immediately after we started the PEC process, indicating that the remaining oxygen in the anolyte (after the deaeration with argon gas) was consumed by the intermediates. By contrast, a continuous increase was observed in the oxygen concentration at the beginning of the dark reaction that showed a decrease over time, signalling that the intermediate products consume oxygen faster than it is produced in the OER process. As a result, glyceraldehyde and dihydroxyacetone intermediates were not detected in the anolyte after the dark reaction, similarly to the case of the oxygen saturated anolyte after the PEC oxidation reaction (Supplementary Fig. 14).

Combining two high-value processes

To examine the product distribution of CO_2R as a function of potential, we switched again to CO_2 feed on the cathode side. The products were analysed by gas chromatography during potentiostatic experiments at five different potentials (Fig. 7). All measurements showed around 90% FE for CO and the rest of the charge was used for H_2 production. In light of these results, the custom-designed photoanode–dark cathode cell can produce high-value products on both sides, and it is suitable to
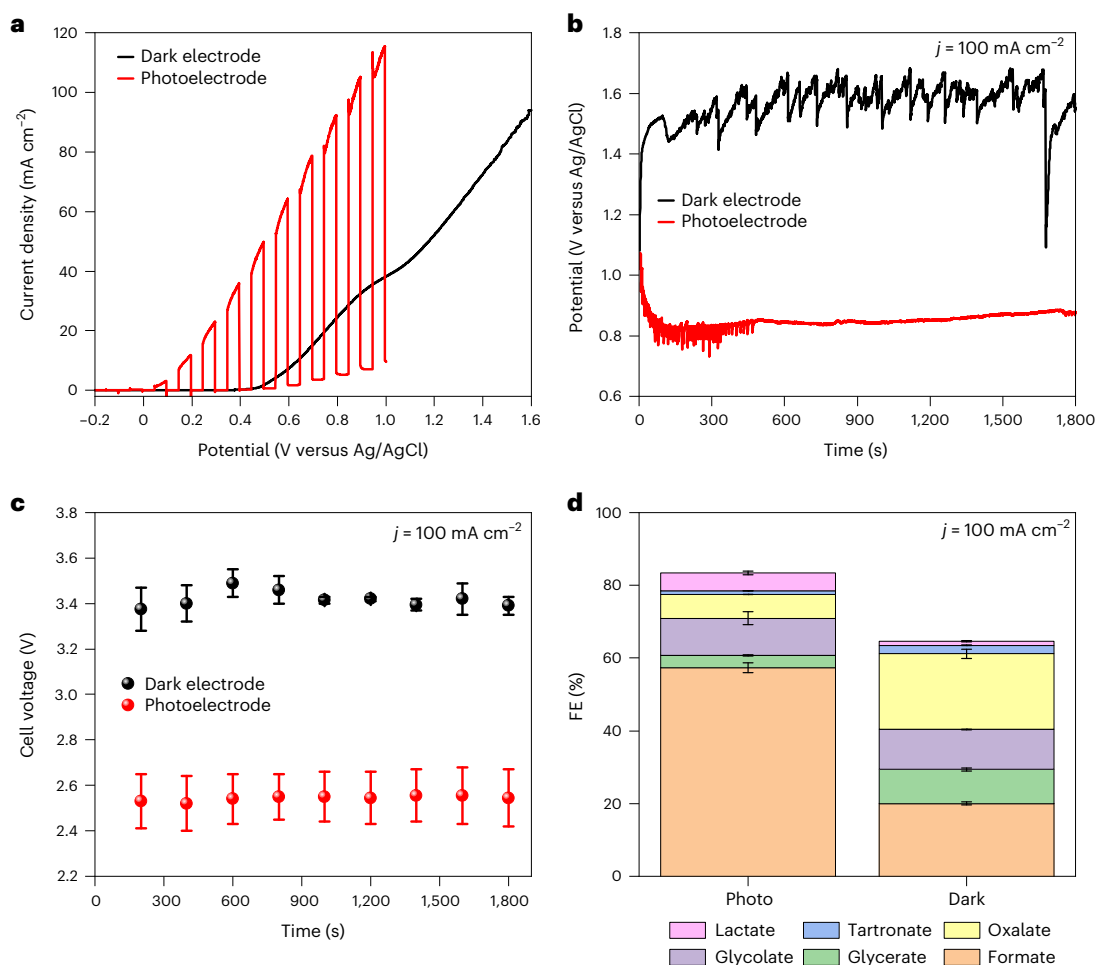
Fig. 6 | Comparison of dark and photooxidation of glycerol. a, Linear (photo) voltammograms recorded with 10 mV s^{-1} sweep rate. **b**, Anode potential differences during 30 min galvanostatic experiments at current density $j = 100$ mA cm^{-2}. **c**, Cell voltage differences during 30 min galvanostatic experiments at 100 mA cm^{-2}. **d**, Product distribution in the anolyte after 30 min galvanostatic experiments at 100 mA cm^{-2}. The anolyte was 0.5 M glycerol containing 1.0 M CsOH. HER was performed on the cathode side using 25 cm^3 min^{-1} argon flow, while the anolyte flow rate was 10 cm^3 min^{-1}. The temperature of the cell and the anolyte was 35 °C. The error bars represent the standard deviation from the mean, originated from three separate measurements performed on three different Ni/Si and Ni sheet containing electrodes. The missing FE in **d** is related to dihydroxyacetone, glyceraldehyde and oxygen.

perform other electrochemical processes by selecting the appropriate catalysts and parameters for the desired products. Note, however, that the synergistic coupling between the two half reactions is extremely important for long-term operation. In this regard, NiOOH is not the best choice as the anode catalyst when CO$_2$R takes place on the cathode side. Protons are generated in the anodic glycerol oxidation reaction (Supplementary Equation (8)), which are completely neutralized in the case of HER, by the hydroxide ions passing through the membrane. This results in a constant pH during the experiment (the pH was 13.54 before and 13.41 after the HER experiment at 1.0 V anode potential). In the case of CO$_2$R at the cathode, the ion conduction is maintained by carbonate ions[62]. In this case, the neutralization of protons formed at the anode can only partially take place, which ultimately leads to a decrease in the anolyte pH (from 13.54 to 12.65 at 1.0 V anode potential: detailed description and the chemical equations in the Supplementary Note 5). As a result, the NiOOH starts to dissolve from the surface of the Si[39], which leads to a gradual decrease in the photocurrent (NiOOH is not only the catalyst but also acts as a protection layer against the corrosion of Si)[63]. This process was confirmed by long-term potentiostatic experiments at two different potentials (0.6 and 1.0 V versus Ag/AgCl) under 10 sun, and at 1.0 V (versus Ag/AgCl) under 1 sun irradiation,

both with HER and CO$_2$RR as the cathode reaction (Supplementary Fig. 15). The photoelectrode retained 80% of the initial photocurrent after 3 hours with HER under concentrated sunlight, while only 30% remained under CO$_2$RR conditions (Supplementary Fig. 15a,b). The observed 3 hour stability with HER is promising, as only the catalyst deposition prevents the photocorrosion of Si (no additional protection strategies were used). To determine the contribution of concentrated solar irradiation to the degradation process, we performed 8 hours of photoelectrolysis under 1 sun with both HER and CO$_2$R (Supplementary Fig. 15c). Clearly, the lower irradiation intensity and therefore the lower photocurrent density resulted in an increased stability of the electrode assemblies. The slower dissolution rate of the catalyst in the case of CO$_2$R resulted in 75% photocurrent retention after 4 hours. The concentration of dissolved Ni was also quantified in the anolyte after these experiments by inductively coupled plasma mass spectrometry. Four times higher Ni^{2+} concentration was determined in the anolyte when CO$_2$R was the cathode reaction, which proves the accelerated dissolution of Ni catalyst.

We performed another 3 hour potentiostatic experiment coupled with product analysis, where argon gas was fed to the cathode in the first 2.2 hours, then the argon was changed to CO$_2$ (Supplementary
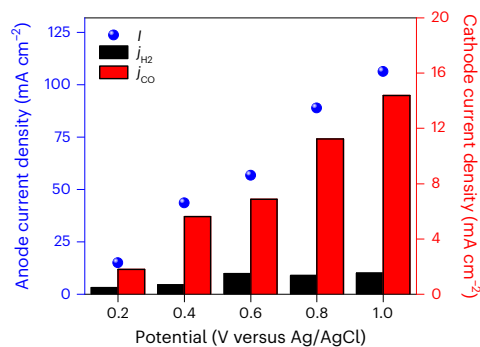
Fig. 7 | Distribution of CO₂R products. The products were detected by gas chromatography during potentiostatic measurements at five different potentials. Constant parameters: 35 °C, 0.5 M glycerol in 1.0 M CsOH, 2 cm³ min⁻¹ anolyte flow rate, 25 cm³ min⁻¹ CO₂ flow rate. The difference in the anodic and cathodic current density is caused by the different electrode area as detailed in the experimental section (the total current is equal). I indicates the total current density (that is, equal to the current density at the anode as the surface of the photoelectrode is 1 cm²); j_{H_2} and j_{CO} denote the partial current density of H_2 and CO, respectively, at the cathode.

Fig. 16). Until water reduction occurred on the cathode side, the photocurrent was stable and not surprisingly 100% hydrogen was detected. As soon as the gas was changed to CO_2, the photocurrent started to decrease, and CO became the main product of the gas phase.

To prevent or at least slow down the dissolution process, the anolyte was non-recirculated and fresh solution was continuously supplied to the anode when CO₂R occurred on the cathode side (Figs. 2 and 7). In these experiments the anolyte flow rate was decreased to 2 cm³ min⁻¹.

Selection of the appropriate catalyst and semiconductor
The onset potential difference of glycerol- and water photooxidation is small (200 mV) on Ni catalyst (Fig. 3a), which means that the electricity consumption is almost the same in the two processes. This is surprising, especially if we compare the thermodynamic potential difference of the two electrochemical reactions, which is around 0.8 V (ref. 24). This indicates that Ni is not the best catalyst in glycerol oxidation, while it shows notable activity in OER. Using noble metal catalysts, the overpotential of glycerol oxidation can be lowered[7], and the reaction can be performed even without C–C cleavage (that is, mainly C3 products can be obtained: Supplementary Note 6 and Supplementary Fig. 17). These catalysts, however, are quickly poisoned by the reaction intermediates (mainly by the adsorbed CO)[7]. To mitigate the poisoning effect of CO, the anode catalyst should either bind CO weakly but still oxidize glycerol, or it should oxidize the adsorbed CO at low potentials. In this regard, PtRu seems to be a good candidate to overcome the mentioned limitation of pure noble metals[64]. When using a PtRu catalyst we observed a sudden current decrease during glycerol oxidation starting from −0.15 V (versus Ag/AgCl), both in the electrochemical and PEC processes (black and red curves in Fig. 8a, respectively). There are two possible events that occur at the mentioned potential: Pt oxide formation on the surface, which is not active in glycerol oxidation[64] and/or dissolution of Ru from PtRu that hinders its beneficial properties[65]. In addition to the current drop, the PEC reaction started at the same potential as the dark current onset (black and red curves in Fig. 8a and red curve in Supplementary Fig. 18a), showing there was no photopotential under illumination (to be discussed later). By contrast, Ni showed remarkable stability, but the overpotential of glycerol oxidation was roughly 1.0 V (blue curve in Fig. 8a and Supplementary Fig. 18a). This overpotential can be halved by using a Ni-covered Si photoelectrode (green curve in Fig. 8a and Supplementary Fig. 18a), but the efficiency

still lags behind PtRu that shows roughly 0.5 V lower onset potential even in the dark.

To explain the observations in Fig. 8a, thermodynamics should be considered. Beside the catalyst, the valence band position and the flatband potential (which is close to the Fermi level, E_F) of the semiconductor should also be carefully examined. In principle, the semiconductor is suitable to perform an oxidation reaction if the energy level of holes (that is, the valence band position) is more positive (on the potential scale versus Ag/AgCl) than the redox potential of the given process. In this regard, Si seems to be a suitable candidate for glycerol oxidation (Supplementary Fig. 18a) with presumably high selectivity, since the thermodynamic driving force for the parasitic OER is low (the valence band position is close to the theoretical onset potential of water oxidation). A catalyst, however, must be used on its surface to efficiently extract the light generated holes from the valence band (that is, enhanced charge separation). When the Fermi level of the catalyst lies more negative on the vacuum scale than the E_F of the semiconductor (this is the situation in the case of Ni), electrons will transfer from the semiconductor to the catalyst until thermodynamic equilibrium is reached[66]. As a result, the E_F of Ni/Si will be situated at more negative potential on the vacuum scale compared to the E_F of bare Si (Supplementary Figs. 18b and 19a). By contrast, the E_F of PtRu lies very close to the original E_F of Si, thus there will be negligible change in its value in the case of PtRu/Si photoelectrode (Supplementary Figs. 18b and 19b). These energetics also dictate the observed photopotential under illumination, as described in Supplementary Fig. 19.

The theoretical photocurrent onset is determined by the flatband potential that is, in principle, equal to the position of the original E_F before reaching equilibrium[67]. This is in good agreement with our results (Supplementary Fig. 18a) as the determined flatband potential (−0.71 V versus Ag/AgCl derived from Mott–Schottky analysis, Supplementary Fig. 20) was close to the E_F of bare Si (−0.57 ± 0.08 V versus Ag/AgCl). In the case of semiconductor–metal junctions, however, the photocurrent onset can appear at notably higher (more positive) potentials depending on the photopotential and the kinetic overpotential[67,68]. The photopotential is determined by the potential difference between the electron and hole quasi-Fermi levels of the illuminated semiconductor, which can be affected by the catalyst (Fig. 8b). As the difference between the quasi-Fermi levels of electrons and holes is negligible in the PtRu/Si electrode, no photopotential can build up (Fig. 8b)[69]. This is the reason why the photo- and dark current onset potentials are identical in this case. On the other hand, the photopotential is roughly 0.45 V on Ni-covered Si; accordingly, the photocurrent onset is negatively shifted by 0.45 V in the case of Ni/Si, compared to the process on Ni sheet (green and blue curves in Fig. 8a). Even though a photopotential can be observed on Ni/Si, the onset potential of the photocurrent is positively shifted compared to PtRu/Si. This is because of the large (1.0 V) kinetic overpotential of glycerol oxidation on Ni that can be reduced by the value of the photopotential[70].

Operation at higher total current
To test whether the photocurrent scales with the geometrical surface, the size of the photoelectrode was increased by sixfold (a detailed description can be found in the Supplementary Note 7). The achievable maximum photocurrent density decreased by 30% with the sixfold increase of the electrode surface (Supplementary Fig. 21), which signals that the scale-up either makes the contact preparation more difficult (imperfect contact) or that the extraction of the light generated charge carriers becomes sluggish because of the longer lateral transport. It should be mentioned, however, that the total photocurrent was roughly 250 mA with the larger electrode even under 4 sun of irradiation.

Conclusions
A continuous-flow PEC cell was designed to perform the direct photooxidation of glycerol combined with the dark electroreduction
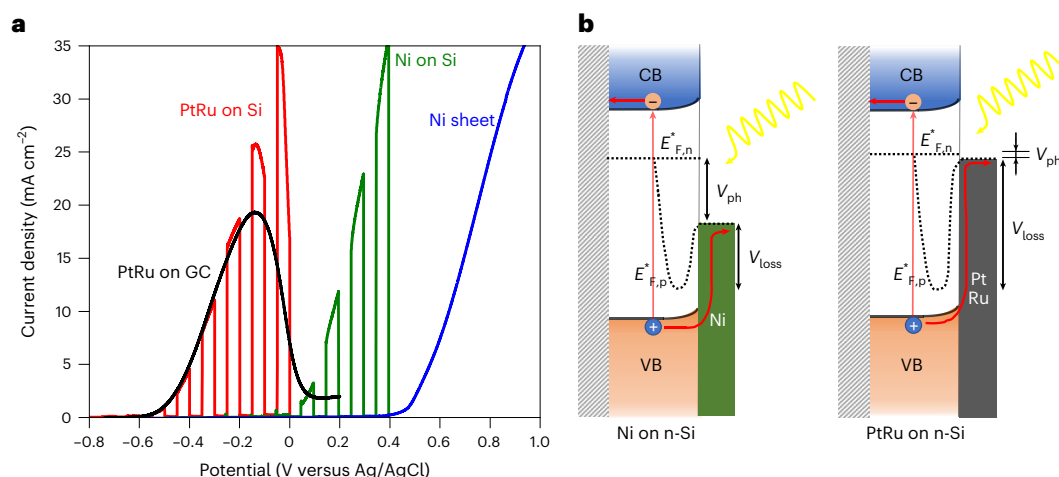
Fig. 8 | Effect of the catalyst on electrochemical activity and on the value of photopotential. a, Comparison of the onset potential of electrochemical and PEC glycerol oxidation using PtRu and Ni catalysts. **b**, Schematic band energy diagram of the illuminated Ni/Si and PtRu/Si photoanodes. $E^*_{F,n}$ and $E^*_{F,p}$ represent the quasi-Fermi levels of electrons and holes, respectively, while the difference between them shows the measurable photopotential (V_{ph}). CB, conduction band; GS, glass carbon; VB, valence band; V_{loss}, loss of photopotential.

of water or CO_2. A photocurrent density of more than 110 mA cm^{-2} was achieved under 10 sun irradiation using a high-performance Si-based photoanode. The reaction rate and the selectivity of the oxidation process was controlled by the operational parameters. We found that simply by varying the cell temperature, the anode potential (the band bending and therefore the number of holes reaching the surface) and/or the concentration of glycerol (the amount of the reactant), we could shift the reaction pathway to produce larger amount of the desired product, although still a product mixture forms. We compared the PEC and electrochemical oxidation of glycerol at the same current density, and we found a notably different product distribution. The phenomenon can be explained by the at least 0.45 V lower cell voltages (rooted in the anodic half-cell) in the case of the illuminated photoelectrode that ultimately leads to higher selectivity (glycerol oxidation without parasitic OER). The PEC scenario is therefore an exceptional case of the Butler–Volmer relationship where the current and the overpotential can be decoupled to a certain extent. With properly paired semiconductor–catalyst assemblies, bias free operation can be possible at high current densities, and such studies are in progress. Further studies will also assess the challenges of limited stability, by engineering the semiconductor(–protecting layer)–catalyst interface.

Methods
Materials
All chemicals were purchased from commercial suppliers (Sigma-Aldrich, VWR International), and were of at least analytical grade and were used without further purification. MilliQ grade (ρ = 18.2 MΩ cm) ultrapure deionized water was used to prepare all the solutions.

Electrode preparation
In all experiments with the flow PEC cell, a Si-based photoelectrode or a Ni sheet containing electrode was used on the anode side, while a catalyst covered carbon cloth was used on the cathode side.

The photoelectrode consisted of two parts: a copper-based PCB as the contact and a single side polished n-type Si wafer (UniversityWafer, Inc., dopant P, resistivity 0.1–0.5 Ω cm, thickness 500 μm) as the photoactive material. To have good contact between the two components, several steps were performed during the preparation. First, the backside (unpolished side) of the Si wafers was scratched by a sandpaper, then these electrodes were sonicated in acetone, isopropanol and

deionized water for 5–5 min. To remove the oxide layer from the surface of the Si, the electrodes were immersed in buffered oxide etchant solution for 3 min and then were rinsed with water. The buffered oxide etchant solution contained 10 g of NH$_4$F·HF, 15 ml H$_2$O and 2.5 ml of concentrated hydrogen fluoride. As the next step, the PCB and the Si were heated to 200 °C on a hotplate, then an indium piece was placed on them. The indium melts at this temperature and becomes spreadable. Both the backside of the Si and the PCB contact were covered by the melted metal, then the two parts were put together and cooled down to room temperature. With this process a robust contact can be prepared. The indium containing parts of the contact around the Si was covered with epoxy before the catalyst deposition. After the epoxy dried, the Ni catalyst was deposited using a two-step potentiostatic method: −1.4 V (versus Ag/AgCl) was applied for 1 s, then −1.0 V (versus Ag/AgCl) was used up to 25 mC cm^{-2} charge density. The aqueous solution contained 0.1 M NiSO$_4$ and 0.1 M H$_3$BO$_3$ and was stirred during the deposition. The Ni catalyst layer prepared thus consisted of nanoparticles (Supplementary Fig. 22). By contrast, PtRu nanoparticles (carbon supported PtRu with a molar ratio of 1:1 from Tanaka) were spray coated on the surface of the preheated Si wafer or glassy carbon electrode at 100 °C from a 1:1 isopropanol:water suspension (2.5 mg cm^{-3}), together with 15 wt% ionomer (Sustainion XB-7) that acted as a binder. In this case, the catalyst loading was ~25 μg cm^{-2}. In the dark measurements, Ni sheet (Sigma-Aldrich, ≥99.9%, thickness 125 μm) was used instead of the Si wafer and it was placed on the indium covered PCB in the same way.

Silver nanoparticles (d_{avg} < 100 nm, Sigma-Aldrich) were used as the catalyst on the cathode side. These particles were spray coated on preheated carbon cloth (gas diffusion layer) (ELAT-LT1400) at 100 °C from a 1:1 isopropanol:water suspension (25 mg cm^{-3}), together with 15 wt% ionomer (PiperION I-46). The spray-coating was performed with a hand-held airbrush with compressed air carrier gas and the catalyst loading was 1.0 ± 0.1 mg cm^{-2}.

The PEC cell
The PEC cell used for all electrochemical experiments contains the following components (from right to left in Fig. 1): an end ring that holds the plexiglass window in its position; a Si photoanode on a PCB held together by an indium layer; a polypropylene mesh that acts as a spacer to hold the AEM in place beneath the photoanode; a photoanode holder that contains the anode current collector, the reference electrode and the anolyte in- and outlet; a PTFE-reinforced 32 μm

thick PiperION TP-85 AEM from Versogen; a GDE with its catalyst layer facing the membrane; a spacer element to set the compression ratio of the GDE (together with the polypropylene mesh); a cathode current collector with a concentric flow-pattern with a central inlet and an outlet on the perimeter and finally an end plate with a fluid chamber that allows the cell temperature to be precisely controlled (tempered water is continuously flowed through the chamber and the actual cell temperature can be tracked by a thermometer). The whole cell is held together by four M5 bolt screws (0.45 Nm torque was applied). All currents were normalized to the photoanode surface, which was 1 cm², while on the cathode side the active surface was circular and 2.9 cm in diameter, resulting a geometrical surface of 6.6 cm². As a result, the current density was always 6.6 times lower on the cathode side when the experiments were performed with the 1 cm² photoelectrode (Fig. 7). We also carried out experiments (Supplementary Fig. 21) where the anode and the cathode surface were similar (6.25 cm²).

Characterization methods

The dynamic viscosity of the anolyte was measured in a cone–plate geometry (CPE-40 cone) with an LVDV-II+ ProC/P viscometer (Brookfield). The viscosity values were obtained by fitting the shear stress versus shear rate data (that showed a linear relationship) with the Bingham model.

The thickness of the deposited Ni film was identified by atomic force microscopy (AFM) using an NT-MDT Solver AFM microscope (Supplementary Fig. 23), operated in the tapping mode with a silicon tip on a silicon nitride lever (Nanosensors, Inc., SSS-NCH-type 15 μm long silicon needle with 10° half cone angle and 2 nm radius curvature).

The surface morphology and the coverage were examined (Supplementary Fig. 22) by a Thermo Fisher Scientific Apreo C scanning electron microscope equipped with Everhart–Thornley detector. The microscope was operated at 25 pA current and 10 kV acceleration voltage.

The light absorption and reflection properties of the Ni layer were measured with an Agilent 8453 UV–vis diode array spectrophotometer in the range of 300–1,100 nm (Supplementary Fig. 24).

The valence band position of Si and the Fermi level of bare and catalyst coated Si electrodes were determined both by Kelvin probe microscopy and ultraviolet photoelectron spectroscopy (UPS) (Supplementary Fig. 25a–c). Kelvin probe microscopy measurements were performed using a KP Technology APS04 instrument. First, the contact potential difference was measured between the sample and the tip of the Kelvin probe after electric equilibrium was reached (Supplementary Fig. 25a). The Fermi level was calculated from these data. During the measurement, a 2 mm diameter gold alloy-coated tip was vibrated above the sample surface at a constant height (roughly 1 mm) and amplitude (0.2 mm), with a constant frequency (70 Hz). Ambient pressure UV–photoelectron spectroscopy measurements were carried out with a stationary Kelvin probe tip (Supplementary Fig. 25b). The sample surface was illuminated with a 4–5 mm spot size, variable energy UV light source. The UV light generates an electron cloud from the semiconductor if $h\nu \geq E_{VB}$ (where h is the Planck constant and ν is the frequency of the light). This is followed by the formation of secondary ions that can be collected by the Kelvin probe tip: thus, a current is measured. In the case of semiconductors, there is a cube root dependence of this current on the excitation energy. The intersection of the baseline and the rise in the cube root of the photoemission current can be then related to the valence band of a given semiconductor. Before measurements, the Fermi level of the gold alloy-coated tip was determined by measuring the Fermi level of a reference Ag target ($E_{F,Au\,tip} = 4.60$ eV).

X-ray photoelectron spectroscopy (XPS) measurements were performed with a SPECS instrument equipped with a PHOIBOS 150 MCD 9 hemispherical analyser. The analyser was operated in fixed transmission mode with 40 eV pass energy for acquiring survey scans.

For the high-resolution scans 20 eV pass energy was used. Al Kα radiation ($h\nu = 1,486.6$ eV) was used as an excitation source and operated at 150 W power. Ten scans were averaged to get a single high-resolution spectrum (Supplementary Figs. 26 and 27). Charge referencing was performed for the adventitious carbon C 1s peak (284.8 eV). For spectrum evaluation, the CasaXPS commercial software package was used.

UPS was performed with He(I) excitation (21.22 eV) and 10 V external bias was applied to the samples to accelerate secondary electrons to the analyser. The recorded UPS spectra were corrected for additional He(I) satellites. The work function of the samples was determined from the second derivative of the secondary electron cutoff at large binding energies and the Fermi level of metallic samples was extracted from fitting the first derivative of the small binding energy region to a Gaussian function. The valence band of Si was determined from fitting the onset of the small binding energy region (Supplementary Fig. 25c).

The conduction band position was calculated using the optical bandgap value of Si (1.14 eV) obtained from Tauc analysis (Supplementary Fig. 25d). Diffuse reflectance spectra were recorded with a Shimadzu UV-3600 Plus spectrophotometer between 400 and 1,600 nm.

Electrochemical experiments and product analysis

During the electrochemical measurements the argon or CO₂ flow rate on the cathode side was controlled with a Bronkhorst F-201CV type mass-flow controller, while an Agilent ADM flow meter was used to measure the flow rate of the gas outlet. The anolyte (40 cm³) was continuously purged with argon gas during the experiments and was circulated in the anode compartment using a peristaltic pump (Ismatec). All electrochemical experiments were performed using a Metrohm Autolab PGSTAT302 type potentiostat–galvanostat in a standard three-electrode setup. The Si-based photoelectrode functioned as the working electrode, the silver containing carbon cloth (GDE) as the counterelectrode, and a Ag/AgCl wire as a pseudoreference electrode, which was located on the anode side. In this configuration, the potential of the photoelectrode was controlled during the measurements and the total cell voltage between the anode and the cathode was measured and recorded by a voltmeter.

PEC experiments were carried out using a solar simulator (Sciencetech SL-50A-WS, AM 1.5) as the light source with a power density of 1,000, 400 or 100 mW cm⁻², In all cases, the sweep rate was kept at 10 mV s⁻¹, while the light-chopping frequency was 0.20 Hz.

Electrochemical impedance spectra were measured in a two-electrode setup (between the anode and the cathode) at open circuit voltage with 10 mV root-mean-square perturbation in the 200 kHz down to the 10 Hz frequency range, with ten points per frequency decade.

For the Mott–Schottky analysis, impedance spectra were recorded at different potentials between 100 kHz and 10 Hz in a batch cell and the flatband potential was determined at 1 kHz. Before each measurement, a pretreatment step was applied at the given potential for 1 min.

The composition of the products on the cathode side was analysed using a Shimadzu GC-2010 Plus type instrument, equipped with a barrier discharge ionization detector. A Restek ShinCarbon ST column was used for the separation with 6.0 grade Helium carrier gas. An automatized six-port valve was used to take samples in regular time intervals.

The effect of three different parameters was examined on the product distribution of the anolyte: the cell temperature, the glycerol concentration in the anolyte and the anode potential. During these measurements, only one parameter was changed while the others were constant. The basic parameters were: 1.0 mol dm⁻³ CsOH and 0.5 mol dm⁻³ glycerol containing anolyte, 35 °C cell temperaure, 0.6 V anode potential, 10 cm³ min⁻¹ anolyte flow rate and 25 cm³ min⁻¹ Ar/CO₂ flow rate.

The anolyte composition after the electrochemical experiments was analysed by a Bruker Avance Neo 500 NMR spectrometer and

a Shimadzu Prominence LC-20AD liquid chromatograph equipped with a ReproGel H (9.0 μm, 300 × 8 mm) column and an SPD-M20A diode array detector. The semiquantitative analysis of glyceraldehyde and dihydroxyacetone was carried out by UV–vis spectroscopy, using an Agilent 8453 UV–vis diode array spectrophotometer. In the case of NMR samples, 450 μl of ten times diluted anolyte and 50 μl of phenol and dimethylsulfoxide containing D_2O were mixed in the NMR tubes. The one-dimensional ^1H spectrum was measured using a solvent presaturation method to suppress the water peak[71]. During the high-performance liquid chromatography (HPLC) measurements, 5 mM sulfuric acid eluent was used with a flow rate of 0.5 ml min^{-1} and the column temperature was 55 °C. Before the HPLC analysis, 1 ml undiluted anolyte and 250 μl of 2.0 M sulfuric acid were mixed and 20 μl of sample was injected into the column from this mixture. The parasitic oxygen formation was monitored during the measurements by an Orion 3 Star Clark-type oxygen sensor. Before these experiments, the anolyte was carefully deaerated by argon gas, then the electrolyte container was closed to exclude the dissolution of oxygen from the air. FE values were calculated from the amount of charge passed to produce each product divided by the total charge passed (a detailed description can be found in the Supplementary Note 2).

To determine the amount of products that have crossed over the AEM from the anode to the cathode during the reactions, the cathode compartment was washed with 5 × 2 cm^3 of a solvent mixture of 25% (v/v) isopropanol in water. This mixture wets the GDE properly without dissolving its polytetrafluoroethylene content or damaging the AEM. These solutions were then analysed by NMR and HPLC.

The error bars on the figures represent the standard deviation from the average (mean), originated from three separate measurements performed with three different electrodes.

Data availability

The authors declare that all data supporting the findings of this study are presented in the article and Supplementary Information or are available from the corresponding author upon reasonable request.

References

1. Meyer, T. H., Choi, I., Tian, C. & Ackermann, L. Powering the future: how can electrochemistry make a difference in organic synthesis? *Chem* **6**, 2484–2496 (2020).
2. Heard, D. M. & Lennox, A. J. J. Electrode materials in modern organic electrochemistry. *Angew. Chem. Int. Ed.* **59**, 18866–18884 (2020).
3. Vass, Á., Endrődi, B. & Janáky, C. Coupling electrochemical carbon dioxide conversion with value-added anode processes: an emerging paradigm. *Curr. Opin. Electrochem.* **25**, 100621 (2021).
4. Na, J. et al. General technoeconomic analysis for electrochemical coproduction coupling carbon dioxide reduction with organic oxidation. *Nat. Commun.* **10**, 5193 (2019).
5. *Platinum Group Metal Management* (Johnson Matthey, 2024); http://www.platinum.matthey.com/prices/price-charts
6. Kortlever, R., Shen, J., Schouten, K. J. P., Calle-Vallejo, F. & Koper, M. T. M. Catalysts and reaction pathways for the electrochemical reduction of carbon dioxide. *J. Phys. Chem. Lett.* **6**, 4073–4082 (2015).
7. Fan, L. et al. Recent progress in electrocatalytic glycerol oxidation. *Energy Technol.* **9**, 2000804 (2021).
8. Yao, T., An, X., Han, H., Chen, J. Q. & Li, C. Photoelectrocatalytic materials for solar water splitting. *Adv. Energy Mater.* **8**, 1800210 (2018).
9. Kumar, B. et al. Photochemical and photoelectrochemical reduction of CO_2. *Annu. Rev. Phys. Chem.* **63**, 541–569 (2012).
10. Endrődi, B. et al. Continuous-flow electroreduction of carbon dioxide. *Prog. Energy Combust. Sci.* **62**, 133–154 (2017).
11. Kumaravel, V., Bartlett, J. & Pillai, S. C. Photoelectrochemical conversion of carbon dioxide (CO_2) into fuels and value-added products. *ACS Energy Lett.* **5**, 486–519 (2020).
12. Yan, Z., Ji, M., Xia, J. & Zhu, H. Recent advanced materials for electrochemical and photoelectrochemical synthesis of ammonia from dinitrogen: one step closer to a sustainable energy future. *Adv. Energy Mater.* **10**, 1902020 (2020).
13. Ardo, S. et al. Pathways to electrochemical solar-hydrogen technologies. *Energy Environ. Sci.* **11**, 2768–2783 (2018).
14. Spitler, M. T. et al. Practical challenges in the development of photoelectrochemical solar fuels production. *Sustain. Energy Fuels* **4**, 985–995 (2020).
15. Tilley, S. D. Recent advances and emerging trends in photo-electrochemical solar energy conversion. *Adv. Energy Mater.* **9**, 1802877 (2019).
16. He, J. & Janáky, C. Recent advances in solar-driven carbon dioxide conversion: expectations versus reality. *ACS Energy Lett.* **5**, 1996–2014 (2020).
17. Vilanova, A., Lopes, T., Spenke, C., Wullenword, M. & Mendes, A. Optimized photoelectrochemical tandem cell for solar water splitting. *Energy Storage Mater.* **13**, 175–188 (2018).
18. Irtem, E. et al. A photoelectrochemical flow cell design for the efficient CO_2 conversion to fuels. *Electrochim. Acta* **240**, 225–230 (2017).
19. Castro, S., Albo, J. & Irabien, A. Photoelectrochemical reactors for CO_2 utilization. *ACS Sustain. Chem. Eng.* **6**, 15877–15894 (2018).
20. Ampelli, C., Centi, G., Passalacqua, R. & Perathoner, S. Synthesis of solar fuels by a novel photoelectrocatalytic approach. *Energy Environ. Sci.* **3**, 292–301 (2010).
21. Urbain, F. et al. A prototype reactor for highly selective solar-driven CO_2 reduction to synthesis gas using nanosized earth-abundant catalysts and silicon photovoltaics. *Energy Environ. Sci.* **10**, 2256–2266 (2017).
22. Homayoni, H., Chanmanee, W., De Tacconi, N. R., Dennis, B. H. & Rajeshwar, K. Continuous flow photoelectrochemical reactor for solar conversion of carbon dioxide to alcohols. *J. Electrochem. Soc.* **162**, E115–E122 (2015).
23. Kalamaras, E. et al. A microfluidic photoelectrochemical cell for solar-driven CO_2 conversion into liquid fuels with CuO-based photocathodes. *Faraday Discuss.* **215**, 329–344 (2019).
24. Verma, S., Lu, S. & Kenis, P. J. A. Co-electrolysis of CO_2 and glycerol as a pathway to carbon chemicals with improved technoeconomics due to low electricity consumption. *Nat. Energy* **4**, 466–474 (2019).
25. Antón-García, D. et al. Photoelectrochemical hybrid cell for unbiased CO_2 reduction coupled to alcohol oxidation. *Nat. Synth.* **1**, 77–86 (2022).
26. Liu, D. et al. Selective photoelectrochemical oxidation of glycerol to high value-added dihydroxyacetone. *Nat. Commun.* **10**, 1779 (2019).
27. Liu, Z.-Q., Huang, S., Ouyang, T., Zheng, B.-F. & Dan, M. Enhanced photoelectrocatalytic activities for CH_3OH to HCHO conversion on Fe_2O_3/MoO_3: Fe-O-Mo covalency dominates the intrinsic activity. *Angew. Chem.* **60**, 9546–9552 (2021).
28. Zhou, Z. et al. Selective photoelectrocatalytic tuning of benzyl alcohol to benzaldehyde for enhanced hydrogen production. *Appl. Catal. B Environ.* **286**, 119868 (2021).
29. Cha, H. G. & Choi, K. S. Combined biomass valorization and hydrogen production in a photoelectrochemical cell. *Nat. Chem.* **7**, 328–333 (2015).
30. Bender, M. T., Yuan, X. & Choi, K. S. Alcohol oxidation as alternative anode reactions paired with (photo)electrochemical fuel production reactions. *Nat. Commun.* **11**, 4594 (2020).
31. Wang, C. et al. A novel electrode for value-generating anode reactions in water electrolyzers at industrial current densities. *Angew. Chem. Int. Ed.* **62**, e202215804 (2023).

32. Pan, Y. et al. Renewable formate from sunlight, biomass and carbon dioxide in a photoelectrochemical cell. *Nat. Commun.* **14**, 1013 (2023).

33. Choi, D. S., Kim, J., Hollmann, F. & Park, C. B. Solar-assisted ebiorefinery: photoelectrochemical pairing of oxyfunctionalization and hydrogenation reactions. *Angew. Chem.* **132**, 16020–16024 (2020).

34. Vilanova, A. et al. Solar water splitting under natural concentrated sunlight using a 200 cm^2 photoelectrochemical-photovoltaic device. *J. Power Sources* **454**, 227890 (2020).

35. Khan, M. A., Al-Shankiti, I., Ziani, A., Wehbe, N. & Idriss, H. A stable integrated photoelectrochemical reactor for H$_2$ production from water attains a solar-to-hydrogen efficiency of 18% at 15 suns and 13% at 207 suns. *Angew. Chem.* **132**, 14912–14918 (2020).

36. Tembhurne, S., Nandjou, F. & Haussener, S. A thermally synergistic photo-electrochemical hydrogen generator operating under concentrated solar irradiation. *Nat. Energy* **4**, 399–407 (2019).

37. Boutin, E. et al. Photo-electrochemical conversion of CO$_2$ under concentrated sunlight enables combination of high reaction rate and efficiency. *Adv. Energy Mater.* **12**, 2200585 (2022).

38. Endrődi, B. et al. Multilayer electrolyzer stack converts carbon dioxide to gas products at high pressure with high efficiency. *ACS Energy Lett.* **4**, 1770–1777 (2019).

39. Vass, Á. et al. Local chemical environment governs anode processes in CO$_2$ electrolyzers. *ACS Energy Lett.* **6**, 3801–3808 (2021).

40. Kwon, Y., Lai, S. C. S., Rodriguez, P. & Koper, M. T. M. Electrocatalytic oxidation of alcohols on gold in alkaline media: base or gold catalysis? *J. Am. Chem. Soc.* **133**, 6914–6917 (2011).

41. Wu, J. et al. Steering the glycerol electro-reforming selectivity via cation–intermediate interactions. *Angew. Chem. Int. Ed.* **61**, e202113362 (2022).

42. Thorson, M. R., Siil, K. I. & Kenis, P. J. A. Effect of cations on the electrochemical conversion of CO$_2$ to CO. *J. Electrochem. Soc.* **160**, F69–F74 (2013).

43. Endrődi, B. et al. Operando cathode activation with alkali metal cations for high current density operation of water-fed zero-gap carbon dioxide electrolysers. *Nat. Energy* **6**, 439–448 (2021).

44. Wang, Q. et al. CoNiFe-LDHs decorated Ta$_3$N$_5$ nanotube array photoanode for remarkably enhanced photoelectrochemical glycerol conversion coupled with hydrogen generation. *Nano Energy* **89**, 106326 (2021).

45. Raptis, D., Dracopoulos, V. & Lianos, P. Renewable energy production by photoelectrochemical oxidation of organic wastes using WO$_3$ photoanodes. *J. Hazard. Mater.* **333**, 259–264 (2017).

46. Tang, R. et al. Fabrication of MOFs' derivatives assisted perovskite nanocrystal on TiO$_2$ photoanode for photoelectrochemical glycerol oxidation with simultaneous hydrogen production. *Appl. Catal. B Environ.* **296**, 120382 (2021).

47. Lee, Y. et al. Surface-modified Co-doped ZnO photoanode for photoelectrochemical oxidation of glycerol. *Catal. Today* **359**, 43–49 (2021).

48. Vo, T. G., Kao, C. C., Kuo, J. L., Chiu, C. & Chiang, C. Y. Unveiling the crystallographic facet dependence of the photoelectrochemical glycerol oxidation on bismuth vanadate. *Appl. Catal. B Environ.* **278**, 119303 (2020).

49. Perini, N. et al. Photoelectrochemical oxidation of glycerol on hematite: thermal effects, in situ FTIR and long-term HPLC product analysis. *J. Solid State Electrochem.* **25**, 1101–1110 (2021).

50. Wu, Y. H., Kuznetsov, D. A., Pflug, N. C., Fedorov, A. & Müller, C. R. Solar-driven valorisation of glycerol on BiVO$_4$ photoanodes: effect of co-catalyst and reaction media on reaction selectivity. *J. Mater. Chem. A* **9**, 6252–6260 (2021).

51. Chong, R., Wang, B., Li, D., Chang, Z. & Zhang, L. Enhanced photoelectrochemical activity of nickel-phosphate decorated phosphate-Fe$_2$O$_3$ photoanode for glycerol-based fuel cell. *Sol. Energy Mater. Sol. Cells* **160**, 287–293 (2017).

52. Lin, C. et al. Photo-electrochemical glycerol conversion over a Mie scattering effect enhanced porous BiVO$_4$ photoanode. *Adv. Mater.* **35**, 2209955 (2023).

53. Li, Y., Wei, X., Chen, L., Shi, J. & He, M. Nickel-molybdenum nitride nanoplate electrocatalysts for concurrent electrolytic hydrogen and formate productions. *Nat. Commun.* **10**, 5335 (2019).

54. Sheng, H. et al. Linear paired electrochemical valorization of glycerol enabled by the electro-Fenton process using a stable NiSe$_2$ cathode. *Nat. Catal.* **5**, 716–725 (2022).

55. Goetz, M. K. K., Bender, M. T. & Choi, K. S. Predictive control of selective secondary alcohol oxidation of glycerol on NiOOH. *Nat. Commun.* **13**, 5848 (2022).

56. Endrődi, B. et al. High carbonate ion conductance of a robust PiperION membrane allows industrial current density and conversion in a zero-gap carbon dioxide electrolyzer cell. *Energy Environ. Sci.* **13**, 4098–4105 (2020).

57. Fleischmann, M., Korinek, K. & Pletcher, D. The oxidation of organic compounds at a nickel anode in alkaline solution. *J. Electroanal. Chem. Interfacial Electrochem.* **31**, 39–49 (1971).

58. Fleischmann, M., Korinek, K. & Pletcher, D. The kinetics and mechanism of the oxidation of amines and alcohols at oxide-covered nickel, silver, copper, and cobalt electrodes. *J. Chem. Soc., Perkin Trans. 2* **31**, 1396–1403 (1972).

59. Dai, C. et al. Electrochemical production of lactic acid from glycerol oxidation catalyzed by AuPt nanoparticles. *J. Catal.* **356**, 14–21 (2017).

60. Kwon, Y., Schouten, K. J. P. & Koper, M. T. M. Mechanism of the catalytic oxidation of glycerol on polycrystalline gold and platinum electrodes. *Chem. Cat. Chem.* **3**, 1176–1185 (2011).

61. Morales, D. M. et al. Electrocatalytic conversion of glycerol to oxalate on Ni oxide nanoparticles-modified oxidized multiwalled carbon nanotubes. *ACS Catal.* **12**, 982–992 (2022).

62. Ma, M., Clark, E. L., Therkildsen, K. T., Dalsgaard, S., Chorkendorff, I. & Seger, B. Insights into the carbon balance for CO$_2$ electroreduction on Cu using gas diffusion electrode reactor designs. *Energy Environ. Sci.* **13**, 977–985 (2020).

63. Kenney, M. J. et al. High-performance silicon photoanodes passivated with ultrathin nickel films for water oxidation. *Science* **342**, 836–840 (2013).

64. Luo, H. et al. Progress and perspectives in photo- and electrochemical-oxidation of biomass for sustainable chemicals and hydrogen production. *Adv. Energy Mater.* **11**, 2101180 (2021).

65. Kormányos, A., Speck, F. D., Mayrhofer, K. J. J. & Cherevko, S. Influence of fuels and pH on the dissolution stability of bifunctional PtRu/C alloy electrocatalysts. *ACS Catal.* **10**, 10858–10870 (2020).

66. Cheng, C., Zhang, W., Chen, X., Peng, S. & Li, Y. Strategies for improving photoelectrochemical water splitting performance of Si-based electrodes. *Energy Sci. Eng.* **10**, 1526–1543 (2022).

67. Mayer, M. T. Photovoltage at semiconductor–electrolyte junctions. *Curr. Opin. Electrochem.* **2**, 104–110 (2017).

68. He, Y., Hamann, T. & Wang, D. Thin film photoelectrodes for solar water splitting. *Chem. Soc. Rev.* **48**, 2182–2215 (2019).

69. Digdaya, I. A., Trześniewski, B. J., Adhyaksa, G. W. P., Garnett, E. C. & Smith, W. A. General considerations for improving photovoltage in metal-insulator-semiconductor photoanodes. *J. Phys. Chem. C.* **122**, 5462–5471 (2018).

70. Liu, R., Zheng, Z., Spurgeon, J. & Yang, X. Enhanced photoelectrochemical water-splitting performance of semiconductors by surface passivation layers. *Energy Environ. Sci.* **7**, 2504–2517 (2014).

71. Kuhl, K. P., Cave, E. R., Abram, D. N. & Jaramillo, T. F. New insights into the electrochemical reduction of carbon dioxide on metallic copper surfaces. *Energy Environ. Sci.* **5**, 7050–7059 (2012).

72. Liu, C. et al. Selective electro-oxidation of glycerol to dihydroxyacetone by a non-precious electrocatalyst–CuO. *Appl. Catal. B Environ.* **265**, 118543 (2020).

Acknowledgements

Author contributions

C.J. conceived and supervised the project. C.J. and A.B. designed all experiments. A.B., D.F. and J.H. carried out all electrochemical and product analysis experiments. G.F.S. performed the XPS and UPS measurements. A.B., E.K., J.H. and C.J. designed the electrodes, the electrochemical cell and the electrolyser system. All authors discussed the results and assisted during manuscript preparation.

Competing interests

The authors declare no competing interests.

Additional information

Supplementary information The online version contains supplementary material available at https://doi.org/10.1038/s41929-024-01134-3.

Correspondence and requests for materials should be addressed to Csaba Janáky.

Peer review information *Nature Catalysis* thanks Ludmilla Steier and the other, anonymous, reviewer(s) for their contribution to the peer review of this work.

Reprints and permissions information is available at www.nature.com/reprints.

Publisher's note Springer Nature remains neutral with regard to jurisdictional claims in published maps and institutional affiliations.